Design Process and Verification of SPMSM for a Wearable Robot Considering Thermal Characteristics Through LPTN

Sung-Woo Hwang, Jun-Woo Chin, and Myung-Seop Lim, *Member, IEEE*

***Abstract*—According to an understanding of wearable robot systems, this article suggests an appropriate design process for surface-mounted permanent magnet synchronous motor (SPMSM) for the joints of wearable robots. The major requirements of SPMSM for the wearable robot are investigated and categorized into the dimensional constraints, electromagnetic performances, and thermal restrictions. Given the defined requirements, the electric motor design process for an actual robot is proposed, considering electromagnetic and thermal characteristics. For thermal analysis, the lumped parameter thermal network (LPTN) is adopted, and the process to compose a precise LPTN for the SPMSM is presented. With given controller and electric motor specifications, the numbers of poles and slots are determined, and fractional-slot concentrated winding is adopted considering the overall behavior of the SPMSM such as torque density and noise and vibration. As a preliminary design, the shape of the rotor including permanent magnets, shape of the stator, and the number of turns are designed via space harmonic analysis which is fast. Subsequently, a detailed design process is performed via finite-element analysis. At this stage, the thermal characteristics considering the driving cycle are analyzed via the LPTN, which is appropriate for parametric design. The final model is determined from electromechanical and thermal viewpoint. Finally, experiments are conducted to validate the proposed design process.**

***Index Terms*—Electric motor design, fractional-slot concentrated winding (FSCW), lumped parameter thermal network (LPTN), multiphysics analysis, space harmonic analysis (SHA), surface-mounted permanent magnet synchronous motor (SPMSM), wearable robot.**

I. Introduction

RECENTLY, wearable robots, which are also known as exoskeleton robots, have been intensively researched in several fields, such as the medical field for rehabilitation, the military and industrial areas where the power assistance technology is required. Wearable robots powered by electric motors are widely adopted because of their compactness, simple structure, and better noise and vibration characteristics compared with those of pneumatic and hydraulic actuators [1], [2]. Although most studies focus not on the electric motor but concentrate on the mechanism of the robot structure or control algorithm [3]–[5]. Nevertheless, optimizing the motor for the robot system significantly affects the system performance and the user experience of the wearable robot [6]. A few studies have examined the electric motor for robots, but their applications are not wearable robots but other types, such as mobile robots or industrial robot arms [7]–[9]. Besides, most of the researches focused on electromagnetic field only. However, the electric motor for wearable robot joints should be designed in consideration of the thermal characteristics simultaneously. Yeo *et al.* [10] and Zhang *et al.* [11] deal with the electromagnetic and thermal multiphysics design. Yeo *et al.* [10], however, concentrate on the effect of the overhang structure of the surface-mounted permanent magnet synchronous motor (SPMSM). Besides, their design process including the electromagnetic and thermal analyses methods are not provided in both studies.

In response to the situation, this article provides pragmatic and useful design method of electric motor for wearable robot joints. First, the criteria that should be considered in the design stage of the electric motor for wearable robot joints are suggested as follows:

1) A pancake shape with large hollow having high power density for compactness and lightness.
2) A low cogging torque and torque ripple for smooth controllability and back-drivability.
3) Low heat transfer from the electric motor to the human body for a good user experience.

Based on the design criteria above, specific requirements are established in Section II, prior to the design process with practical example. To satisfy those multiphysical requirements, the design process involves both electromagnetic and thermal analysis methods. The flow diagram of the proposed process is presented in Fig. 1. An SPMSM, which is advantageous to satisfy the requirements, is adopted [12]–[14]. In the preliminary design, a space harmonic analysis (SHA) is utilized, which is accurate and very fast. It is suitable for the parametric design

Manuscript received November 11, 2019; revised February 5, 2020, April 9, 2020, and June 23, 2020; accepted August 3, 2020. Date of publication August 11, 2020; date of current version April 15, 2021. This work was supported by the National Research Foundation of Korea grant funded by the Korea government (Ministry of Science, ICT, and Future Planning) under Grant 2018R1C1B5085447. Recommended by Technical Editor S. K. Dwivedi and Senior Editor M. Basin. *(Corresponding author: Myung-Seop Lim.)*

The authors are with the Department of Automotive Engineering, Hanyang University, Seoul 04763, South Korea (e-mail: supertramph@hanyang.ac.kr; cjw1254@hanyang.ac.kr; myungseop@hanyang.ac.kr).

Color versions of one or more of the figures in this article are available online at https://ieeexplore.ieee.org.

Digital Object Identifier 10.1109/TMECH.2020.3015561

1083-4435 © 2020 IEEE. Personal use is permitted, but republication/redistribution requires IEEE permission.
See https://www.ieee.org/publications/rights/index.html for more information.

Authorized licensed use limited to: Hanyang University. Downloaded on April 20,2021 at 00:46:59 UTC from IEEE Xplore. Restrictions apply.

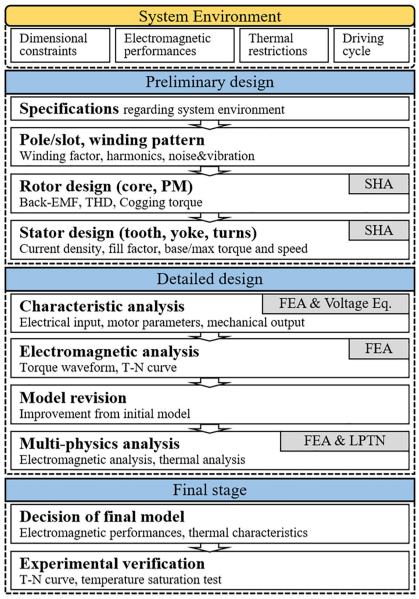

Fig. 1. Flow diagram of the design process.

[15]. The initially designed model is further investigated from the perspective of the electromagnetic performances via a finite-element analysis (FEA), and the thermal characteristics are examined using a lumped parameter thermal network (LPTN). The FEA has been widely used for electromagnetic fields and has been verified in the field. It exhibits very high accuracy. The LPTN, which is significantly faster than other methods such as computational fluid dynamics and thermal FEA, is used. The LPTN is useful for the parametric design because the thermal parameters in the thermal network are calculated according to the dimensions of the electric motor. The accuracy of the LPTN is acceptable when the composition of the thermal network and determination of thermal coefficients are properly conducted. In this point of view, an appropriate method for constructing the LPTN for the SPMSM, including the compartmentalization of the motor shape and determination of heat transfer coefficients is proposed in Section III. Considering the electromagnetic and thermal performance, a detailed design method is proposed, and the final model is determined. Subsequently, the final model is manufactured to validate the proposed design process. The results of a load test (torque-speed-current curve), and a thermal test (temperature trends) demonstrate the validity and effectiveness of the proposed design process.

II. Requirements of Motor for Wearable Robot Joints

As mentioned previously, there are three main criteria when designing the electric motor for wearable robots. First, the power density should be high, and a thin shape with large hollow ensures system compactness. Second, since the motion of the robot joint directly interacts with the human body, the cogging torque and the torque ripple should be minimized for back-drivability. This is also important for control perspective. Third, the electric motor is located very close to the human body, and there is no

TABLE I
Requirements of Motor for Wearable Robot Joints

Contents		Unit	Value
Stator outer diameter		mm	≤ 76.0
Rotor inner diameter		mm	≥ 36.7
Axial length		mm	≤ 18.0
Max. current		A_{pk}	15.0
DC link voltage		V_{DC}	24.0
Max. torque		Nm	≥ 0.75
Rated speed		rpm	2,800
Max. speed		rpm	$\geq 4,000$
Torque ripple (at rated)		%	≤ 2.0
Housing temperature	a. 30min. normal cycle	°C	≤ 35
	b. 3min. max. load	°C	≤ 35

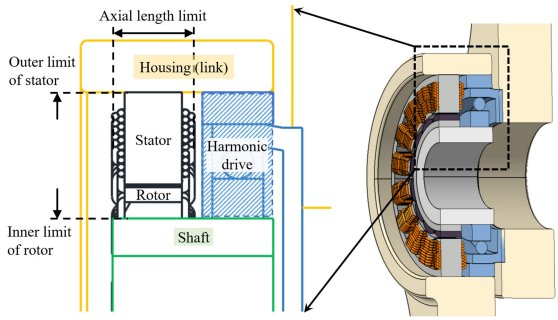

Fig. 2. Layout concept of the wearable robot joint system.

forced cooling system. Thus, the heat generated by the electric motor is directly transferred to the human body. This causes discomfort to the user, which is contrary to the fundamental purpose of wearable robots. Based on the aforementioned aspects, the requirements are divided into the following three categories. Those requirements are discussed with a quantitative example organized in Table I. The specific application in this case is a hip joint of a wearable robot for rehabilitation.

A. Dimensional Constraints

The commonly adopted layout of the robot joints is shown in Fig. 2. It consists of two links (i.e., housings), an electric motor, a harmonic drive, and a shaft. Given the structure of the joint system, the size of the motor is constrained by three dimensions. First, the inner diameter of the rotor core should be larger than the diameter of the shaft, which is same as the inner diameter of the harmonic drive. Second, the outer diameter of the stator core should be smaller than the inner diameter of the housing (i.e., link). This dimension is same as the outer diameter of the harmonic drive. Third, the axial length of the electric motor, including the end coil height, is limited by the layout of the joint. The specific dimensional constraints of the case considered in this article are presented in Table I.

B. Electromagnetic Performance

As the purpose of the wearable robot is to assist the user's motion by means of the torque, an electric motor is required to achieve the target performance of the mechanical output under a given electrical input from the inverter. The electromagnetic

Authorized licensed use limited to: Hanyang University. Downloaded on April 20,2021 at 00:46:59 UTC from IEEE Xplore. Restrictions apply.

performance is defined as a category that combines mechanical output and electrical input requirements. As shown in Table I, the system is driven by a 24-V battery, and the maximum current from the inverter to the electric motor is 15.0 A_{pk}. The required mechanical output performance, i.e., the torque and speed, is determined by the joint system performance and the harmonic drive. The required maximum torque exceeds 0.75 Nm, from 0 to 2800 rpm. Constant power control should be available from the rated speed of 2800 to 4000 rpm. Furthermore, the torque ripple must be minimized to ensure a good user experience and back-drivability. Additionally, the cogging torque should be investigated.

C. Thermal Restrictions

The wearable robot that is also known as the exoskeletal robot is worn on human body. Additionally, the structure of the wearable robot simply consists of electric motors, inverters, and links. Therefore, the heat generated from the motor and inverter is directly transferred to the human body. Given that the wearable robot is used by workers in industrial field and by the patients in medical field, an unpleasant feeling during long-period use can be considered as a fatal defect. Thus, the temperature of the housing should be lower than 35 °C which is a temperature slightly lower than that of the human body under two conditions. The first condition involves operating the electric motor with a normal driving cycle for 30 min, repeatedly. The second condition is stall state which involves operating the electric motor with maximum load for 3 min. This corresponds to the situation of holding heavy load for a long time. In this condition, the motor generates its maximum torque without rotation. The temperatures of the coil and permanent magnets should be simultaneously investigated to confirm the motor performance because degradation occurs in those parts at high temperature.

III. Composition of LPTN for SPMSM

The LPTN is utilized in motor design owing to its high computation speed and adequacy for the parametric design with reasonable accuracy [16]. However, the accuracy of the LPTN depends on how properly the designer handles the LPTN, e.g., composing the thermal network and calculating the thermal coefficients. In this respect, methods for compartmentalizing the SPMSM into lumped parameters and determining the thermal parameters, such as the heat transfer coefficients, are presented, in this section. After all thermal coefficients are determined, the LPTN is solved based on the linear differential equation as expressed in (1) for all nodes [16]

$$C_i \frac{dT_i}{dt} = \frac{1}{R_{ji}} (T_j - T_i) + \dot{Q}_i \tag{1}$$

where C_i is the thermal capacitance of node i, T_i, T_j are ith and jth node temperature, respectively, R_{ji} is the thermal resistance between two adjacent nodes i and j, and $\dot{Q}_i$ is loss at node i.

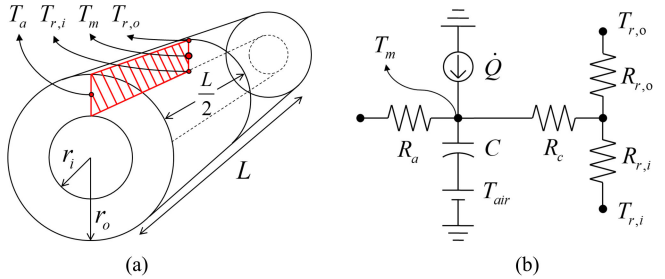

Fig. 3. Fundamental element for each part.

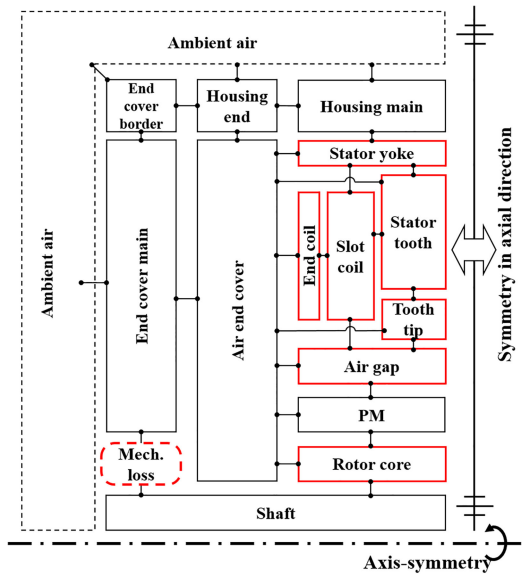

Fig. 4. Compartmentalized LPTN for SPMSM.

A. Compartmentalization

Essentially, the LPTN is based on the assumption that the subject has cylindrical hollow shape as shown in Fig. 3(a). The assumption is appropriate for the case of the SPMSM. The thermal network of the fundamental element is shown in Fig. 3(b). Additionally, it is assumed that the thermal characteristics are symmetrical in the axial direction from the center to both of the opposite ends. Furthermore, according to the axis-symmetry shape of the SPMSM, it can be assumed that there is no heat flow in the circumferential direction. There is an exception in the case of heat flow between the stator tooth and the coil because the parts are located next to each other in the circumferential direction. However, the heat inside a part (i.e., lump) never flows in the circumferential direction. A schematic of the compartmentalized parts and their connection network is shown in Fig. 4. The red boxes indicate the parts that contain heat sources. Iron losses occur in the stator yoke, stator tooth, stator tooth tip, and rotor core. The coil where copper loss occurs is subdivided into the slot coil and the end coil to accurately predict the temperature of the coil.

B. Determination of Thermal Coefficients

The accuracy of thermal analysis using the LPTN depends on the precise determination of the thermal coefficients. The

Authorized licensed use limited to: Hanyang University. Downloaded on April 20,2021 at 00:46:59 UTC from IEEE Xplore. Restrictions apply.

TABLE II
THERMAL COEFFICIENTS

Classification	Location	Dependent on	Values	Ranges
Convective heat transfer coefficient	Environment	Cooling method, dimension, state of flow	27.8 (radial), 31.4 (axial)	5-50 [17], [18]
	Air gap	Rotation speed, state of air flow	105@1030 rpm	5-300 [19]
	Rotor end	Rotation speed, state of air flow	30@1030 rpm	5-300 [19]
	Stator end	Cooling type, rotation speed, state of air flow	15.5	15.5-300 [19], [20]
Contact conductance	Housing - stator	Contact state, material, pressure	5500	500-6000 [21], [22]
Thermal conductivity	Coil	Contact state, impregnated method, existence of varnish, material, pressure	2.4	0.5-3 [22], [23]

thermal coefficients used in this article were determined via the following steps:

1) The ranges of the thermal coefficients were set based on references as shown in Table II [17]–[23].
2) Based on the data of temperature saturation test using an SPMSM model with the size and manufacturing methods similar to those of the model to be designed, the thermal coefficients were tuned within the appropriate ranges.
3) As described in Section IV, the thermal analysis was conducted via the LPTN using the thermal coefficients tuned in the previous step.

Among the thermal coefficients, the thermal conductivity of the coil has the highest uncertainty, owing to the complex structure of the coil. The axial thermal conductivity of the coil is almost identical to the thermal conductivity of copper. However, the radial and circumferential thermal conductivities of the coil differ from the thermal conductivity of copper because the heat is transmitted through the copper, insulation, and impregnation which correspond to air in this case. Therefore, the thermal conductivity of the coil was considered as the equivalent thermal conductivity, as proposed in [23].

C. Consideration of Driving Cycle

The motion of the wearable robot joint, with regard to the torque and the rotation speed, is not constant and varies over time, and the thermal characteristics can be affected by the driving cycle. Therefore, the impact of the driving cycle on the thermal behavior of the electric motor was investigated. The electric motor designed in this article is assumed to be applied to various joints of the wearable robot. Among the joints, the hip joint is operated under the most severe conditions, thus, the driving cycle of the hip joint is applied to the thermal analysis.

The temperature trends of the housing, end coil, and teeth based on time when the electric motor is operated with the driving cycle of the hip joint are shown in Fig. 5. As well as the result when the actual driving cycle is applied, a substitutive condition is contained in the graph. In this condition, the root mean square (rms) value of the input current, which is periodically time-varying, substitutes the driving cycle. In the larger scale graph (left side), it is difficult to determine the difference between the two conditions. By magnifying the graph (right side), the small difference that corresponds to approximately ±0.1 °C is observed. However, the difference is negligible.

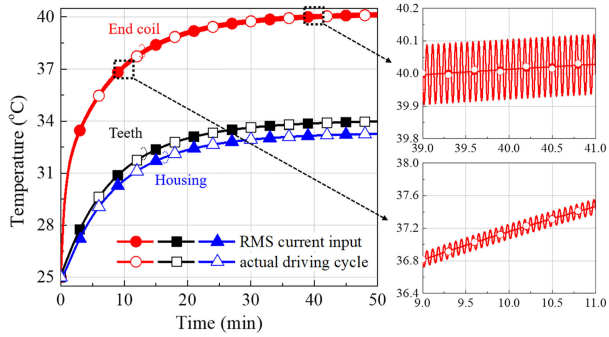

Fig. 5. Comparison of thermal analysis results between the actual driving cycle and RMS value conditions.

D. General Rules for the Thermal Design

In general, since it is not common to use special material or innovative manufacturing methods, it is difficult to improve the heat transfer rate within each part or between parts of motor. Thus, the thermal design of electric motor is performed by dealing with the losses. Under limited size and with similar grades of material, the total loss (i.e., heat sources) cannot be decreased significantly. Therefore, it is important to adequately distribute the heat sources. The major heat sources of the electric motor which can be adjusted are the copper loss in the coils and iron loss in the core. Since these losses are not independent, only copper loss is chosen as control variable. The copper loss is directly related to the current density of the coils. Therefore, it is controlled by changing the size of the conductor. The shape of the slot is changed accordingly. Subsequently, the iron loss is changed due to the changed shape of the core. The optimum temperature distribution is selected considering the thermal restrictions referred in Section II. The practical design process is presented in the Section IV.

IV. DESIGN PROCESS

In this section, the design process of the SPMSM is presented by considering the requirements for the wearable robot joint. First, the preliminary design is conducted using the SHA. Then, the electromagnetic performance of the initial model is evaluated via FEA. By comparing the analysis results with the requirements, the improvement direction is determined, and improved models are suggested. Subsequently, a final model that most adequately satisfies all types of requirements is determined by

Authorized licensed use limited to: Hanyang University. Downloaded on April 20,2021 at 00:46:59 UTC from IEEE Xplore. Restrictions apply.

investigating the electromagnetic performance and the thermal behaviors of the improved models.

A. Preliminary Design

The first step of the electric motor design involves determining the numbers of poles and slots, which are related to the winding pattern. For the sinusoidal current feeding of the inverter, one of the recommendations is to have more than 15 instances of switching in an electrical period. Taking the carrier frequency of the inverter and the target maximum speed of the electric motor into account, the number of poles is limited to 30. The numbers of poles and slots significantly affect the characteristics of the electric motor, such as the winding factor, cogging torque, and noise and vibration characteristics. The winding pattern-related considerations that should be included in the design of the electric motor for the wearable robot joint are as follows:

1) High torque density: high winding factor.
2) Short-end coil height: tooth-coil winding (coil pitch of one-slot pitch).
3) Low cogging torque: large least common multiple of the numbers of poles and slots.
4) Good noise and vibration characteristics.

First, with regard to compactness, the torque density (or the power density) should be high. Thus, the winding factor should be high. Second, with regard to compactness, a short end coil height causes the electric motor to exhibit a short axial length. Thus, nonoverlapping concentrated winding, also known as a coil-tooth winding, having a coil pitch of one-slot pitch is preferred. Third, the cogging torque should be minimized for back-drivability and smooth motion. The cogging torque is proportional to the least common multiple of the numbers of poles and slots [24]. Fourth, noise and vibration characteristics are important for the user comfort. Therefore, the vibration order of the radial magnetic force should be high [25]. Given the aforementioned considerations, the numbers of poles and slots are determined as 14 and 18, respectively.

For the case of wearable robot joint, the main dimensions of the motor including stator outer diameter, rotor inner diameter, and axial length are determined by the system structure as shown in Table I. The next step involves designing the rotor core and the PMs using SHA [26]. To analyze electromagnetic field, a shape of motor is simplified and then the governing equation is solved analytically via SHA [27], [28]. The shape of the PMs is determined via the eccentricity, pole angle, and thickness, as shown in Fig. 6. The rotor shape is designed by considering the characteristics of the electric motor such as the back electromotive force (BEMF), the total harmonic distortion (THD) of the BEMF, and the cogging torque. The pole pitch depends on the number of the poles. The pole angle is determined as the optimum value with regard to the motor characteristics. As shown in the graphs in left side of Fig. 7, the optimum value of the pole angle to pole pitch ratio is determined as 0.92, where the phase BEMF is maximized and the cogging torque is minimized while the THD of the phase BEMF is in a high range. After the ratio is fixed, the eccentricity is set as 16 mm where the phase BEMF is not maximized although the THD of the phase BEMF

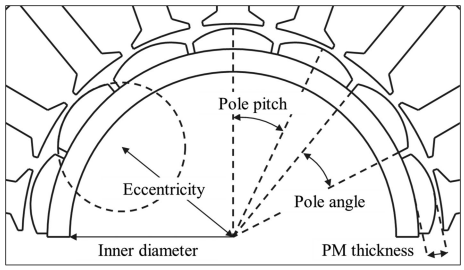

Fig. 6. Design parameters of the rotor.

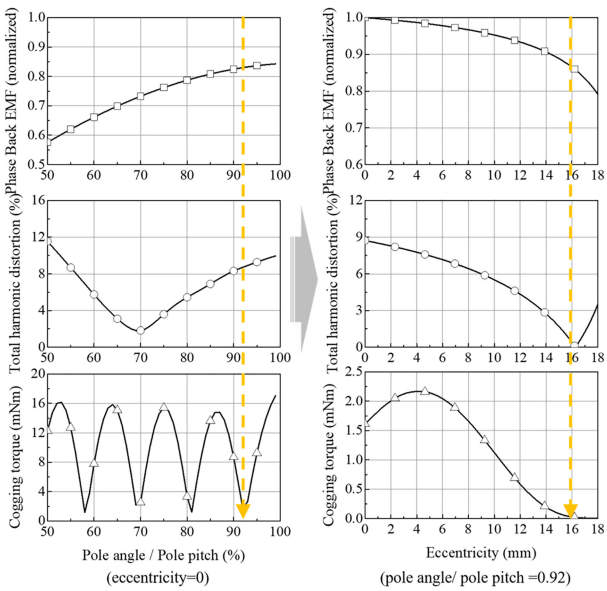

Fig. 7. Design of the PM shape using space harmonic analysis.

and the cogging torque are minimized as shown in the graphs in right side of Fig. 7.

After the field design, the proper value of the phase BEMF is calculated to satisfy the electromagnetic requirements, which are related to the mechanical output and electrical input as follows:

$$P = T \cdot \omega \leq 3 e_{\mathrm{ph}} I \tag{2}$$

$$e_{\mathrm{ph}} \leq V_{\mathrm{ph}} = \frac{1}{2} V_{\mathrm{dc}} \times \frac{1}{\sqrt{2}} \times \text{Duty ratio} \times \text{PWM factor} \tag{3}$$

where P represents the power, and T, ω, e_{ph}, and I represent the torque (in Nm), rotation speed (in rad/s), rms of the phase BEMF, and rms line current (in $\mathrm{A_{rms}}$), respectively. Additionally, V_{ph} represents the maximum phase voltage that can be fed by the inverter under the direct current (dc) link voltage V_{dc}. The minimum required phase BEMF is calculated using the required mechanical power and the line current, as expressed in (2). The maximum value of the phase BEMF is determined by the terminal voltage limit of the inverter, considering the control method, as expressed in (3). The number of series turns per phase that makes the phase BEMF satisfies the maximum and minimum requirements is determined with the field magnetomotive force analyzed via the SHA.

Authorized licensed use limited to: Hanyang University. Downloaded on April 20,2021 at 00:46:59 UTC from IEEE Xplore. Restrictions apply.

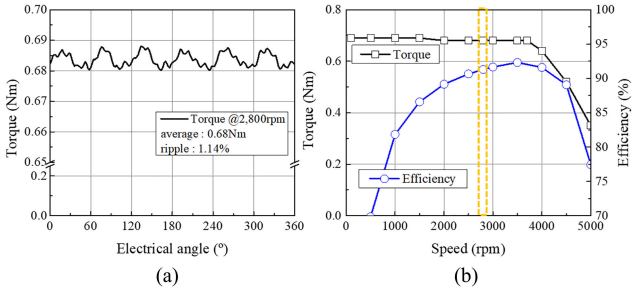

Fig. 8. Mechanical performance of the initial model. (a) Torque waveform at rated point. (b) Torque-speed curve.

The next step involves designing the shape of the slot. First, the area of the slot is calculated by assuming the current density limit to be 10 A_{rms}/mm^2 and the slot fill factor to be 40%. Subsequently, the widths of the yoke and tooth, at which the reluctance of the stator core magnetic circuit is minimized, are determined with the aforementioned dimensional constraints, including the outer diameter and calculated slot area. The reluctance is calculated with the stator dimensions under the no-load condition; thus, the widths of the yoke and tooth are further adjusted according to the load condition.

The torque waveform of the initial model obtained via two-dimensional (2-D) FEA is shown in Fig. 8(a). The results indicate that the torque ripple was 1.14%, which satisfied the requirement of 2.0%. However, the maximum torque of 0.68 Nm did not satisfy the requirement of 0.75 Nm. As shown in Fig. 8(b), the speed range of the maximum torque reached 3600 rpm which exceeds the limit of 2800 rpm.

B. Detailed Design

According to the initial design, the objective of the detailed design was to increase the maximum torque, acknowledging the decrease in the speed range where the model exhibits its maximum torque. Furthermore, the thermal characteristics of the revised models were simultaneously investigated.

The initial model was designed as marginal in terms of the input voltage, which was proportional to the rotation speed. In this case, an appropriate solution to satisfy the requirements involves increasing the number of series turns per phase. Thus, the number of series turns per phase was increased from 84 (initial model) to 90. Increasing the number of turns in the slot without changing the coil diameter requires a larger slot area and causes the magnetic saturation of the stator core, resulting in a lower efficiency due to iron loss and degradation of the magnetic. To prevent these problems, the decrease in the widths of the tooth and yoke should be minimized by reducing the coil diameter. At this point, two revised models in which the coil diameters are smaller than those of the initial models are suggested. For the coil diameter with the same number of turns, the area of the slot and the shape of the stator are differently designed, in a manner similar to the preliminary design. A load analysis for each model at the rated operating point was conducted via 2-D FEA, and the results are shown in Fig. 9. The results indicate that the magnetic

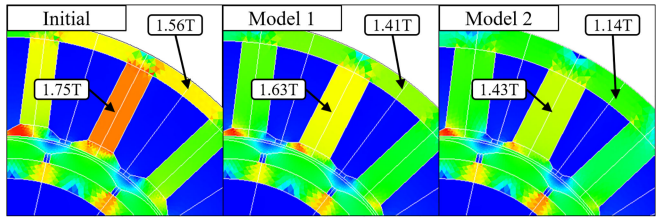

Fig. 9. Comparison of magnetic flux density of stator core at the load of rated. Operating point.

TABLE III
CURRENT DENSITY AND MAXIMUM TORQUE

Models	Current density (A_{rms}/mm^2)		Maximum torque	
	Driving cycle	Max. load	Mean (Nm)	Ripple (%)
Initial	3.79	10	0.68	1.14
Model 1	4.92	13	0.76	1.15
Model 2	5.86	15	0.78	0.72

TABLE IV
LOSSES OF DESIGNED MODELS

Models	Copper loss (W)		Iron loss (W)	
	Driving cycle	Max. load	Driving cycle	Max. load
Initial	3.62	22.01	1.62	0
Model 1	4.72	31.49	1.40	0
Model 2	6.10	36.40	1.16	0

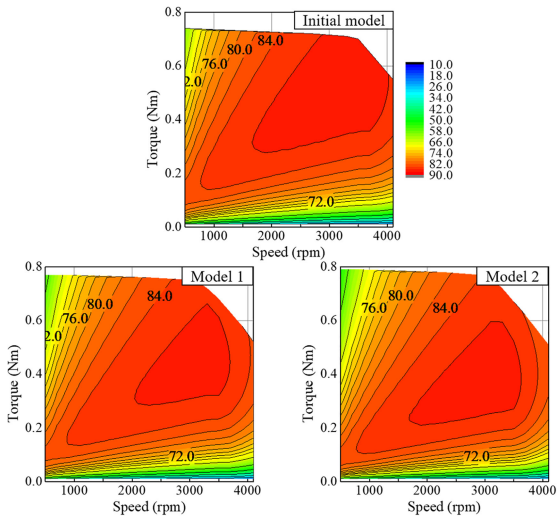

Fig. 10. Efficiency maps.

flux density of the stator core decreased when the area of the slot decreased. The maximum torques and current densities of the models are presented in Table III, and their losses are presented in Table IV. For the second condition, it involves stall condition with maximum load. Thus, the iron losses of all models are zero under the condition since the iron loss is proportional to the electrical frequency. Furthermore, the efficiency maps of three models are shown in Fig. 10. In the efficiency calculation, the copper loss, the iron loss, and the mechanical loss are taken into

Authorized licensed use limited to: Hanyang University. Downloaded on April 20,2021 at 00:46:59 UTC from IEEE Xplore. Restrictions apply.

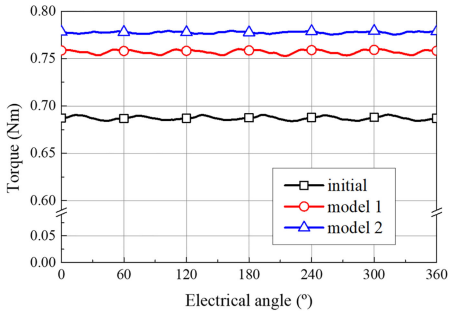

Fig. 11. Torque waveforms of each model at maximum torque.

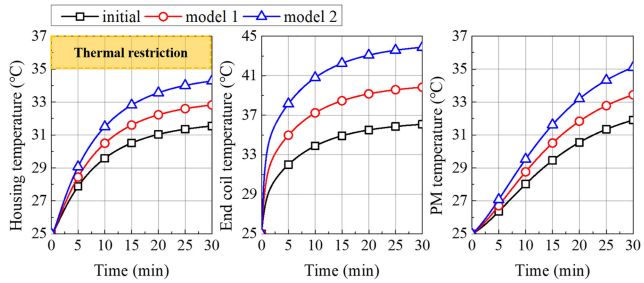

Fig. 12. Temperature trend under the driving cycle.

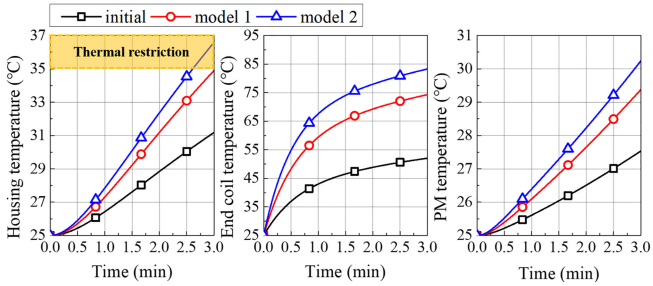

Fig. 13. Temperature trend under the maximum load.

Fig. 14. Final model for the wearable robot joint; 2-D FEA model (left), manufactured sample (center and right).

account. The iron loss is calculated by well-known method using FEA [29]. The measured mechanical loss of an SPMSM having almost same size is applied to this calculation. Regarding the maximum torque, both revised models satisfied the requirement of 0.75 Nm. The increased maximum torque of model 2 was resulted by the mitigation of the magnetic saturation in the stator, as desired through larger widths of the yoke and the teeth [30]. The results show that reducing the slot area causes higher torque constant as shown in Table III. Moreover, the iron loss is reduced as shown in Table IV. However, since the sizes of electric motors for the robot applications are relatively small, the effect of the copper loss on the efficiency is dominant, the efficiency is lowest in the case of Model 2.

At this stage, the thermal characteristics of the models were investigated, because the current density significantly affects the thermal behavior of the electric motor. The LPTN was constructed via the proposed method for three models. As mentioned previously, the temperatures of the housing, end coil, and PM under the normal driving cycle condition and the maximum load condition (15 A_{pk}) were predicted, and considered for decision of the final model.

C. Decision of Final Model

The initial model and two revised models that were designed to satisfy the dimensional constraints were investigated with regard to the electromagnetic and thermal characteristics. As shown in Fig. 11, revised models 1 and 2 satisfied the maximum torque of 0.75 Nm and torque ripple of 2.0%. However, model 2 exhibited a higher maximum torque and lower torque ripple.

Subsequently, the temperature trends were analyzed via the LPTN developed in this article. Thermal analyses were conducted under two conditions which are the normal driving cycle and the stall condition with maximum load. The current densities at those conditions of the models are referred in Table III. First, the condition of the normal driving cycle was applied to the analysis. As mentioned in *C* of Section III, the rms of the torque and rotation speed was applied instead of the actual cycle. The results are shown in Fig. 12. All three models satisfied the thermal restriction that the housing temperature should not exceed of 35 °C after operating 30 min. Model 2 was expected to exhibit greater thermal degradation than model 1 because the increases in the temperatures of the end coil and the PM were larger than those for model 1, although the difference was not significant. As discussed previously, even though the reduced slot area increased the torque constant, the copper loss, which is dominant on the efficiency, caused more severe temperature rise. Second, the models are analyzed under the second condition that the stall state with the maximum torque for 3 min, and the temperature trends are shown in Fig. 13. The temperature in the housing of model 2 increased above 35 °C at 3 min and that of model 1 hardly exceeded 35 °C. Meanwhile, the end coil temperature reached 82.7 °C which was much higher than the housing temperature. It was caused by two factors. First, significant proportion of heat sources were copper loss in the coil due to high current density of 15 A_{rms}/mm^2. Second was slow response of the motor thermal system. Specifically, the heat transfer rate between the coil and stator core through enameled coating of coil and insulation material was much slower than the heat generation rate in the coil by copper loss. Likewise, at the first condition, the temperature difference between the end coil and the housing can be seen in early phase of Fig. 12.

Consequently, model 2 was disqualified with regard to the thermal restriction. Model 1 was selected as the final model. Fig. 14 shows the 2-D FEA modeling and a manufactured sample of the final model. The electromagnetic performance of the final

Authorized licensed use limited to: Hanyang University. Downloaded on April 20,2021 at 00:46:59 UTC from IEEE Xplore. Restrictions apply.

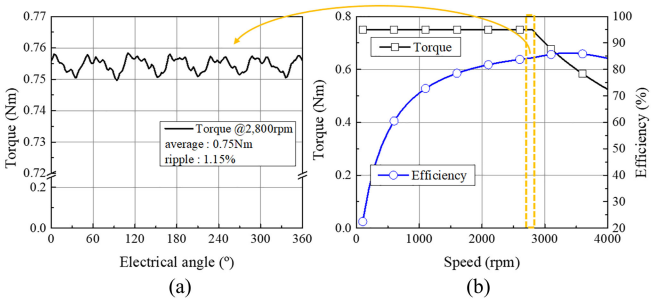

Fig. 15. Mechanical performance of the final model by 2-D FEA. (a) Torque waveform at rated point. (b) Torque-speed curve.

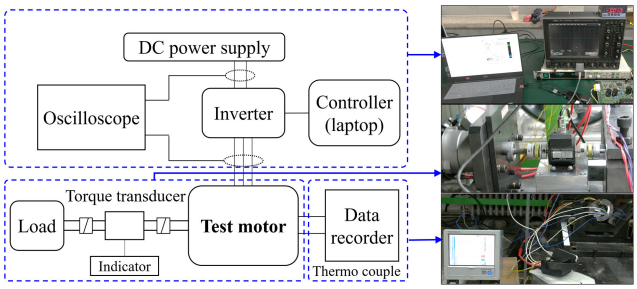

Fig. 16. Experimental set for verification.

TABLE V
CONDITIONS FOR EXPERIMENTAL VERIFICATION

Tests	Parameters	Conditions
Performance test (T-N-I curve)	torque, speed, line current	speed range 0-4000rpm, at room temperature
Thermal test 1	temperatures (end coil, housing)	normal driving cycle
Thermal test 2		twice torque and identical speed of normal driving cycle

model was analyzed via 2-D FEA and the results are shown in Fig. 15. All the requirements were satisfied, including the maximum torque, maximum speed, rated speed, and torque ripple.

V. VERIFICATION

To validate the proposed design process, the experimental set shown in Fig. 16 was used. For torque measurement, a torque transducer, SETECH YDSA-20KC (maximum 1.961 Nm with 0.2% accuracy), and indicator, SETECH YD5553, are used. An oscilloscope LeCroy WaveSurfer 44MXs-B (400 MHz, 5 GS/s) is used to measure the line to line voltage and phase current of the test motor. The temperature data from thermocouple is stored by a data recorder, CP-10, and dc power supply, ITECH IT6512, is used. The test conditions for the experimental verification are presented in Table V. By comparing the torque-speed-current (T-N-I) characteristics of the analysis results with the test results of the manufactured model over whole speed range of the motor, the electromagnetic analysis methods used in the process, such as the SHA and 2-D FEA, were validated. As shown in Fig. 17, the predicted data well agreed with the measured data over the

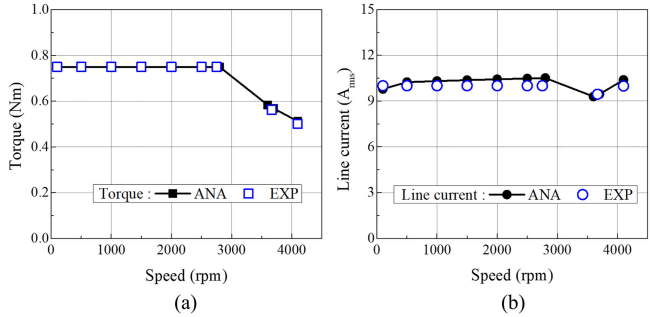

Fig. 17. Verification of electromagnetic FEA. (a) Torque. (b) Line current.

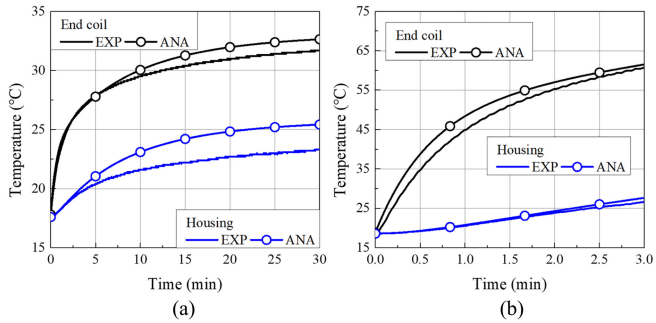

Fig. 18. Comparison of housing and end coil temperature. (a) Normal driving cycle. (b) Twice torque of driving cycle.

whole range. In a constant torque region (0–2800 rpm), the error of the line current increased when the speed increased. It is considered that the error was caused by a factor related to the rotation speed, such as mechanical loss, being overestimated in the design process. The error of the torque in the constant power region (2800–4200 rpm) was negligible. Fig. 18 shows comparisons of the temperature trends. Test was conducted for two conditions, presented in Table V. First, Fig. 18(a) shows the trends under the normal driving cycle. The temperature of the end coil exhibited good agreement between the experiment and analysis, but error of the housing temperature was not negligible. Given that the error of the housing temperature exceeded that of the end coil, it is considered that the heat transfer from the electric motor to the exterior was underestimated in the LPTN. This could be because the temperature measurement was conducted on a test bench in which the volume and contact surface exceeded those of the robot joint system. Due to thermal problem on controller, the second condition, which originally was maximum load in stall state, was changed. It was conducted under the condition that the torque was twice that of the driving cycle and the speed was identical, and the result is shown in Fig. 18(b). The temperature trend predicted via LPTN was very accurate.

VI. CONCLUSION

In response to the insufficient research interest in designing motor for wearable robot joints, an appropriate design method

Authorized licensed use limited to: Hanyang University. Downloaded on April 20,2021 at 00:46:59 UTC from IEEE Xplore. Restrictions apply.

for the SPMSM of a wearable robot joint was presented. According to the features of the wearable robot joint, the design criteria were defined. Based on the criteria, major requirements were established and divided into three categories: the dimensional constraints, electromagnetic performance, and thermal restriction. Subsequently, a design process for the SPMSM based on electromagnetic and thermal analysis was presented. For the preliminary design, the SHA method was used, and 2-D FEA was utilized for detailed design. For a fast and efficient thermal analysis for the parametric design, an LPTN was adopted. For precise prediction of thermal characteristics, pragmatic method to compose the LPTN and way to determine the thermal parameters were provided with example. Through the proposed design process, an electric motor for wearable robot joints are designed. To verify the proposed process, the SPMSM for a wearable robot joint was designed using the proposed process and manufactured.

The designed motor has various advantageous points compared to Kollmorgen TBMS-7615B, which is a target model in the earlier stage. Under the same electrical input 24 V and 15 A, its rated operating point at continuous power was designed slightly lower torque and higher speed region than those of the target model. In dimension point of view, the outer diameter of the stator and inner diameter of the rotor are almost same, but the 9-mm stack length of the designed model is much shorter than 15.24 mm, and 19.30 mm of the target model's stator, and rotor, respectively. Accordingly, the motor weight has been reduced from 400 to 230 g, approximately. Consequently, the power density at continuous power has been improved from 0.575 to 1.0 kW/kg. In the aspect of the torque density, it was improved from 2.11 to 3.41 Nm/kg. This 62% improvement demonstrates the effectiveness of the proposed design process considering electromagnetic and thermal multiphysical field. A direct comparison of the efficiency between the target motor and the designed motor was not conducted. However, assuming similar level of the iron loss, the copper loss can be the indirect index of the efficiency. Since the phase resistance of the designed motor 80 mΩ is much smaller than 180 mΩ of the target model, the energy consumption of the designed motor is expected to be more efficient. The performances stated above are experimentally verified. Also, the thermal experiment results showed that the proposed design process accurately considers the thermal constraints.

Consequently, it is expected that the system performance and user experience of the wearable robot can be enhanced by using an electric motor that is optimally designed for a specific system via the proposed design process.

REFERENCES

[1] H. Al-Fahaam, S. Davis, and S. Nefti-Meziani, "Power assistive and rehabilitation wearable robot based on pneumatic soft actuators," in *Proc. Int. Conf. Methods Models Automat. Robot.*, Sep. 2016, pp. 472–477.

[2] E. Treadway, Z. Gan, C. D. Remy, and R. B. Gillespie, "Toward controllable hydraulic coupling of joints in a wearable robot," *IEEE Trans. Robots*, vol. 34, no. 3, pp. 748–763, Mar. 2018.

[3] A. Parri *et al.*, "Real-time hybrid locomotion mode recognition for lower limb wearable robots," *IEEE/ASME Trans. Mech.*, vol. 22, no. 6, pp. 2480–2491, Dec. 2017.

[4] E. Trigili *et al.*, "Design and experimental characterization of a shoulder-elbow exoskeleton with compliant joints for post-stroke rehabilitation," *IEEE/ASME Trans. Mech.*, vol. 24, no. 4, pp. 1485–1496, Aug. 2019.

[5] T. Kagawa, H. Ishikawa, T. Kato, C. Sung, and Y. Uno, "Optimization-based motion planning in joint space for walking assistance with wearable robot," *IEEE Trans. Robots*, vol. 31, no. 2, pp. 415–424, Apr. 2015.

[6] S. W. Hwang, J. W. Chin, M. S. Lim, and J. P. Hong, "Electromagnetic and thermal multi-physics design of SPMSM for wearable robot," in *Proc. IEEE Int. Conf. Elect. Mach.*, 2018, pp. 724–730.

[7] D. K. Hong, W. Hwang, J. Y. Lee, and B. C. Woo, "Design, analysis, and experimental validation of a permanent magnet synchronous motor for articulated robot applications," *IEEE Trans. Magn* ., vol. 54, no. 3, Mar. 2018, Art. no. 8201304.

[8] R. E. Kim, J. M. Seo, and S. H. Ryu, "Design of permanent magnet motors with distributed and concentrated winding for robot arms," in *Proc. IEEE Int. Conf. Elect. Mach. Syst.*, 2018, pp. 240–243.

[9] W. Zhang *et al.*, "Electromagnetic design of a high torque density permanent magnet motor for biomimetic robot," in *Proc. Int. Conf. Cyborg Bionic Syst.*, 2017, pp. 140–144.

[10] H. K. Yeo, H. J. Park, J. M. Seo, S. Y. Jung, J. S. Ro, and H. K. Jun, "Electromagnetic and thermal analysis of a surface-mounted permanent-magnet motor with overhang structure," *IEEE Trans. Magn.*, vol. 53, no. 6, Jun. 2017, Art. no. 8203304.

[11] W. Zhang, Z. Yu, X. Chen, and Q. Huang, "The magneto-thermal analysis of a high torque density joint motor for humanoid robots," in *Proc. IEEE Int. Conf. Humanoid Robots*, 2018, pp. 112–117.

[12] S. W. Hwang, M. S. Lim, and J. P Hong, "Hysteresis torque estimation method based on iron-loss analysis for permanent magnet synchronous motor," *IEEE Trans. Magn.*, vol. 52, no. 7, Jul. 2016, Art. no. 8204904.

[13] S. F. Toloue, S. H. Kamali, and M. Moallem, "Torque ripple minimization and control of a permanent magnet synchronous motor using multiobjective extremum seeking," *IEEE/ASME Trans. Mech.*, vol. 24, no. 5, pp. 2151–2160, Oct. 2019.

[14] S. K. Kommuri, Y. Park, and S. B. Lee, "High-resistance fault-control in permanent magnet synchronous motors," *IEEE/ASME Trans. Mech.*, vol. 25, no. 1, pp. 271–281, Feb. 2020.

[15] K. H. Shin, H. I. Park, H. W. Cho, and J. Y. Choi, "Analytical calculation and experimental verification of cogging torque and optimal point in permanent magnet synchronous motors," *IEEE Trans. Magn.*, vol. 53, no. 6, Jul. 2017, Art. no. 8106204.

[16] B. H. Lee, K. S. Kim, J. W. Jung, J. P. Hong, and Y. K. Kim, "Temperature estimation of IPMSM using thermal equivalent circuit," *IEEE Trans. Magn.*, vol. 48, no. 11, pp. 2949–2952, Nov. 2012.

[17] Y. A. Cengel and A. J. Ghajar, *Heat and Mass Transfer, Fundamentals and Applications*, 5th ed. New York, NY, USA: McGraw-Hill, 2015.

[18] D. Staton, A. Boglietti, and A. Cavagnino, "Solving the more difficult aspects of electric motor thermal analysis in small and medium size industrial induction motors," *IEEE Trans. Energy Convers.*, vol. 20, no. 3, pp. 620–628, Sep. 2005.

[19] D. A. Howey, P. R. N. Childs, and A. S. Holmes, "Air-gap convection in rotating electrical machines," *IEEE Trans. Ind. Electron.*, vol. 59, no. 3, pp. 1367–1375, Mar. 2012.

[20] P. H. Mellor, D. Roberts, and D. R. Turner, "Lumped parameter thermal model for electrical machines of TEFC design," *IEEE Proc. B Elect. Power Appl.*, vol. 138, no. 5, pp. 205–218, Sep. 1991.

[21] R. Camilleri, D. A. Howey, and M. D. McCulloch, "Experimental investigation of the thermal contact resistance in shrink fit assemblies with relevance to electrical machines," in *Proc. 7th IET Int. Conf. Power Elect. Mach. Drives*, 2014, pp. 1–9.

[22] A. Boglietti, A. Cavagnino, and D. Staton, "Determination of critical parameters in electrical machine thermal models," *IEEE Trans. Ind. Appl.*, vol. 44, no. 4, pp. 1150–1159, Jul./Aug. 2008.

[23] N. Simpson, R. Wrobel, and P. H. Mellor, "Estimation of equivalent thermal parameters of impregnated electrical windings," *IEEE Trans. Ind. Appl.*, vol. 49, no. 6, pp. 2505–2515, Nov./Dec. 2013.

[24] Z. Q. Zhu and D. Howe, "Influence of design parameters on cogging torque in permanent magnet machines," *IEEE Trans. Energy Convers.*, vol. 15, no. 14, pp. 407–412, Dec. 2000.

[25] J. F. Gieras, C. Wang, and J. C. Lai, *Noise of Polyphase Electric Motors*, 1st ed. Boca Raton, FL, USA: CRC Press, 2005.

[26] L. Wu and Z. Q. Zhu, "Analytical modeling of surface-mounted PM machines accounting for magnet shaping and varied magnet property distribution," *IEEE Trans. Magn.*, vol. 50, no. 7, Jul. 2014, Art. no. 8101511.

[27] L. Fang, S. O. Kwon, and J. P. Hong, "Conformal transformation technique for prediction of the magnetic field distribution in an IPM Motor," in *Proc. IEEE Int. Conf. Elect. Mach. Syst.*, vol. 3, Sep. 2005, pp. 2124–2128.

Authorized licensed use limited to: Hanyang University. Downloaded on April 20,2021 at 00:46:59 UTC from IEEE Xplore. Restrictions apply.

[28] Z. Q. Zhu, D. Howe, and C. C. Chan, "Improved analytical model for predicting the magnetic field distribution in brushless permanent-magnet machines," *IEEE Trans. Magn.*, vol. 38, no. 1, pp. 229–238, Jan. 2002.
[29] M. S. Lim, S. H. Chai, J. S. Yang, and J. P. Hong, "Design and verification of 150-krpm PMSM based on experimental results of prototype," *IEEE Trans. Ind. Electron.*, vol. 62, no. 12, pp. 7827–7836, Dec. 2015.
[30] S. W. Hwang, J. H. Sim, J. P. Hong, and J. Lee, "Torque improvement of wound field synchronous motor for electric vehicle by PM-assist," *IEEE Trans. Ind. Appl.*, vol. 54, no. 4, pp. 3252–3259, Jul./Aug. 2018.

Sung-Woo Hwang received the bachelor's degree in mechanical engineering, in 2013, from Hanyang University, Seoul, South Korea, where he is currently working toward the Ph.D. degree in automotive engineering.

His research interests include practical approaches to electric machine design for automotive and robot applications.

Jun-Woo Chin received the bachelor's degree in mechanical engineering, in 2014, from Hanyang University, Seoul, South Korea, where he is currently working toward the Ph.D. degree in automotive engineering.

His research interests include design of electric machines, loss and thermal analysis of electric motor and generator.

Myung-Seop Lim (Member, IEEE) received the bachelor's degree in mechanical engineering, and the master's and Ph.D. degrees in automotive engineering from Hanyang University, Seoul, South Korea, in 2012, 2014, and 2017, respectively.

From 2017 to 2018, he was a Research Engineer with Hyundai Mobis, Yongin, South Korea. From 2018 to 2019, he was an Assistance Professor with Yeungnam University, Daegu, South Korea. Since 2019, he has been with Hanyang University, where he is currently an Assistant Professor. His research interests include electromagnetic field analysis and electric machinery for mechatronics systems such as automotive and robot applications.

Authorized licensed use limited to: Hanyang University. Downloaded on April 20,2021 at 00:46:59 UTC from IEEE Xplore. Restrictions apply.